

Particle and rigidized red blood cell concentration distributions in microchannel flows

Cite as: Phys. Fluids **31**, 082006 (2019); <https://doi.org/10.1063/1.5111201>


Submitted: 24 May 2019 . Accepted: 01 August 2019 . Published Online: 23 August 2019

Kazuya Tatsumi (巽和也) , Shinnosuke Noguchi (野口真之介), Akira Tatsumi (辰巳朗), Reiko Kuriyama (栗山怜子) , and Kazuyoshi Nakabe (中部主敬)

COLLECTIONS

Paper published as part of the special topic on [Selected Articles from the 2018 Micro and Nano Flows Conference](#)

Note: This paper is part of the special issue from the 2018 Micro and Nano Flows Conference.

 This paper was selected as Featured



View Online



Export Citation



CrossMark

ARTICLES YOU MAY BE INTERESTED IN

[Design, modeling, and experimental validation of an acoustofluidic platform for nanoscale molecular synthesis and detection](#)

Physics of Fluids **31**, 082007 (2019); <https://doi.org/10.1063/1.5100149>

[A unified analysis of nano-to-microscale particle dispersion in tubular blood flow](#)

Physics of Fluids **31**, 081903 (2019); <https://doi.org/10.1063/1.5110604>

[Diffusion of ellipsoids in laboratory two-dimensional turbulent flow](#)

Physics of Fluids **31**, 085116 (2019); <https://doi.org/10.1063/1.5113734>



Scilight Highlights of the best new research in the physical sciences

AIP Publishing

LEARN MORE!



Particle and rigidized red blood cell concentration distributions in microchannel flows



Cite as: *Phys. Fluids* **31**, 082006 (2019); doi: [10.1063/1.5111201](https://doi.org/10.1063/1.5111201)

Submitted: 24 May 2019 • Accepted: 1 August 2019 •

Published Online: 23 August 2019



View Online



Export Citation



CrossMark

Kazuya Tatsumi (巽和也),^{a)} Shinnosuke Noguchi (野口真之介), Akira Tatsumi (辰巳朗),
Reiko Kuriyama (栗山怜子), and Kazuyoshi Nakabe (中部主敬)

AFFILIATIONS

Department of Mechanical Engineering and Science, Kyoto University, Kyoto, Japan

Note: This paper is part of the special issue from the 2018 Micro and Nano Flows Conference.

^{a)} Author to whom correspondence should be addressed: tatsumi@me.kyoto-u.ac.jp

ABSTRACT

The motion and concentration distribution of particles and cells in flow are important factors which affect the fluid properties, flow structure, and mass transfer of biological and chemical species in blood vessels and channels. In this study, number density distributions of particles and rigidized red blood cells (RBCs) in a microchannel whose size is comparable to the sizes of the particle and RBCs are measured. Measurements were conducted at several streamwise locations for suspensions of particles and RBCs with hematocrits of the order of 10% and particle sizes of 5 and 8 μm . Analysis of the migration and resulting concentration distribution of the particles and RBCs was conducted using a model that considers the particle–particle collision and fluid dynamic force. As the size of the microchannel is small, the wall effect on the collision and migration of the particles and RBCs was significant. The wall reduced the overlapping area of the particles in collision and their displacement after collision (mobility), which varied the number, location, and magnitude of the maximum peaks observed in the number density distribution. Furthermore, the rotational motion of the rigidized RBCs in the channel flow reduced the effective lengths of the overlapping area and displacement, whereas it produced additional migration at the wall. With these terms added in the model, the number density distributions of the particles and RBCs showed reasonable agreement with those of the measurement. Especially, the number of peaks and their location for the maximum values in the model and measurement matched well.

Published under license by AIP Publishing. <https://doi.org/10.1063/1.5111201>

I. INTRODUCTION

The diffusion and motion of particles and blood cells and the resulting number density (volume fraction, hematocrit) distribution in blood and particle-concentrated flows are essential phenomena in the fields of medicine, biology, and macrofluidic and microfluidic systems. The motion and distribution of the particles and red blood cells (RBCs) affect the fluid viscosity, flow structure, wall shear stress, and mass transfer in the flow and at the walls of the channel and vessel.^{1–10} The motion and number density distribution of the particles and cells can increase or decrease the mass flux of the solute and mobility of other components mixed in the fluid depending on their size relative to that of particles and cells.^{5,7,11–13} The concentration distribution of the particles and cells in the channel will also affect the performance of the sensors, sorting systems, and other functions of the microfluidic devices used in lab-on-a-chip and micro-total analysis systems.^{14–18} Therefore, studies have been keenly performed

to understand the diffusion of particles and blood cells along with their motions and distribution in channel flows and vessels.

The particles in a flow experience various fluid dynamic lift forces depending on the particle diameter-based Reynolds number, the streamline curvature, the shear rate, and wall effects. In a straight channel with simple shear flow or Poiseuille flow, the particles migrate and concentrate at a specific position or distance from the wall depending on the channel Reynolds number.^{19–26} The particle concentration at a specific position can be found in small size channels, owing to the lift force together with the convection by the secondary flows.^{14,15,17,27,28} The streamline curvature formed in curved-, corrugated-, and T-shaped-channels can give additional lift force to make the particles migrate and concentrate at a position different from that of the straight channel.^{29–32} Red blood cells which have biconcave shape and can rotate or perform tank-treading motions receive lift force with a different magnitude and direction compared with spherical particles.^{33–35}

When the particle concentration in the fluid increases, the interaction between the particles becomes significant.^{36–39} Especially, the particle displacement due to the particle–particle collision produces particle migration and affects the particle concentration distribution. Measurements and computations have been conducted in many studies to elucidate the force applied to the particle and the concentration position for highly concentrated flows.^{36–46}

Leighton and Acrivos measured the particle concentration distribution of concentrated suspensions in a Couette flow and proposed a model by modifying the diffusion coefficient of the diffusion term with the collision rate and displacement length based on the shear rate of the flow.⁴⁰ The flux of the particle concentration in the spanwise direction due to the particle–particle collision will rely on the mobility and collision rate. These two will also depend on the local velocity difference and concentration of the particles. Phillips *et al.* introduced the concept of particle concentration flux generated by the particle collision and presented the apparent diffusion term to model this flux in the particle concentration conservation equation.⁴¹ If a velocity gradient exists as in shear flows, particle collision will occur, and movement and diffusion in the spanwise direction will take place even when the particle number distribution is uniform and the concentration gradient is zero, especially for internal flows in which the particle concentration gradient can be zero. Various models have been proposed and expanded based on these principles.^{38,42,47,48} Thus, the particle mobility and concentration distribution in a channel flow have been investigated and evaluated extensively by experiments and numerical computations.

When the channel size decreases and is comparable with the particle size, the confinement of the channel wall significantly affects the particles and RBC concentration distributions in highly concentrated flows compared with the wall-free flows.^{4,10,13,48} The displacement of the particles in collision with other particles and the size of the overlapping area of the two particles are limited by the wall. This will affect the migration velocity of the particles and RBCs and the concentration distribution. As the particle size is comparable with the channel width, the particle mobility in the channel can be more sensitive to the particle size and hematocrit. Moreover, the biconcave shape of the RBC and its rotational motion generate a complex interaction with the wall, which can lead to a migration velocity different to that of the sphere. Few works have been performed investigating the effects of the wall on the particle and RBC migration and concentration distribution in small channels, especially with an experimental approach. Therefore, it is important to measure the effects of the wall, particle size, and hematocrit on the particle and RBC migration to provide insights to understand the concentration distributions and conducting numerical analysis.

In this study, we measure the number density (concentration) distribution of particles and rigidized RBCs suspended in fluids flowing in a straight microchannel. The sizes of the particles are of 5 and 8 μm , which is comparable with the characteristic diameter of the RBC. The channel height and width are approximately 30 μm . The hematocrit of the particles and RBCs is of the order of 10%, which is that of a semidilute or semiconcentrated suspension. The less-packed condition compared with the blood flow is chosen in this study to specifically evaluate the collision effects and increase the measurement accuracy. The RBCs are treated with glutaraldehyde to rigidized the cell membrane and fix the shape. In this study, we

removed the effects of the deformation and tank treading motions on the RBCs to focus on the effects of rotational motions and collisions between the cells and the wall. To discuss several factors affecting the particle migration and concentration flux produced by the particle–particle collision, we conduct an analysis of the particle concentration distribution, employing the model based on that of Phillips *et al.*⁴¹ This model is modified to consider the effects of the wall, RBC shape, and collision with the wall due to the RBC rotation on the overlapping area and displacement of the particle–particle collision. The number density distribution of the particles and RBCs was significantly affected by these factors, and it will be discussed and compared with the measurement result.

First, the measured number density distribution for different streamwise locations, hematocrits, and particle sizes will be shown and discussed. Then, the contributing factors of the particle migration and number density distribution will be shown based on the computation. Finally, the RBC number density distribution of the measurement and computation are compared to discuss the effects of the nonspherical shape of the RBC and rotational motion on the distribution.

II. MEASUREMENT METHOD

A. Experimental apparatus

Figure 1 shows the schematic of the straight microchannel. The channel was divided into three channels at the location of approximately 3.3 mm downstream of the reservoir center. The channels were divided by two plate walls with their leading ends forming an edge shape. This configuration was used to obtain a uniform distribution for the number density of the particles and RBCs at the inlet of the center channel. The measurement was conducted at the center channel. The width and height of the center channel were 28 μm and 27 μm , respectively. The channel was made of polydimethylsiloxane (PDMS; Shin-etsu Chemical Co., KE-106). The channel shape was patterned on the PDMS using SU-8 (Microchem, Su-8 3025) as the mold through the soft lithography process. The PDMS channel was attached to a cover glass to seal and form the channel.

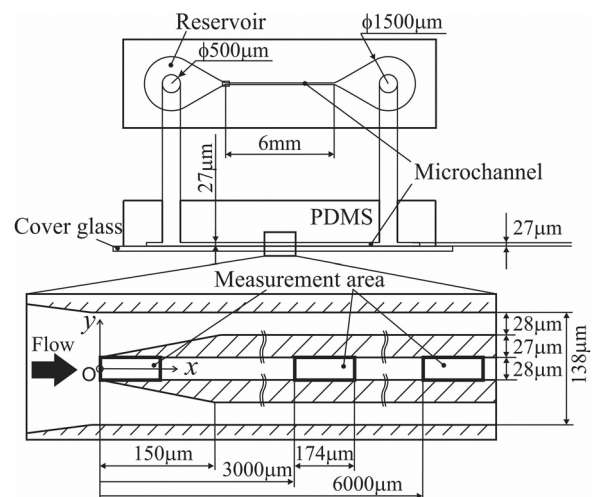


FIG. 1. Schematic of the microchannel and measurement area.

The fluid in which particles and RBCs were mixed was supplied to the channel through a Teflon tube from a fluid pump driven by compressed air. Bubbles formed in the microchannel can change the flow structure significantly and induce clogging of the particles and RBCs. To prevent the generation of the bubbles, we first filled the channel with fluid. After confirming that no bubble existed in the channel, we supplied the working fluid from the inlet to the channel.

The images of the particles and RBCs were measured by using a microscope (Olympus Co., IX-71) and a high-speed video camera (Vision Research, Inc., Phantom V1610). The combination of the camera and objective lens (Olympus Co., UplanSApo100XO) gave us the spatial resolution of $0.28 \mu\text{m}/\text{pixel}$. The focusing depth was $0.62 \mu\text{m}$.⁴⁹ The images of the particles in the channel were measured by epi-illumination imaging, while the images of the RBCs were measured by transillumination imaging. Figure 2 shows the examples of the particle and RBC images measured at the stream-wise position of $x = 3000 \mu\text{m}$ of the center microchannel. The images of the particles and RBCs were analyzed by ImageJ⁵⁰ to obtain the numbers of the particles and RBCs in the area. The numbers of the particles and RBCs at each location in the channel were counted based on their center positions. The numbers then were converted to the number density.

We applied the convolution process to the epi-illumination images of the particles using a ring shape kernel with diameter identical to that of the particles. The images of the particles in focus could be detected accurately, and the particles located in other heights were excluded by this method. This gave us a better result to track the center of the particles located at the channel midheight compared with the case using the transillumination imaging. On the other hand, transillumination imaging was used for RBCs for two reasons. One is that a clear contrast could not be obtained for the outline of the RBCs. The other is that the convolution process was difficult to apply to their complex shape.

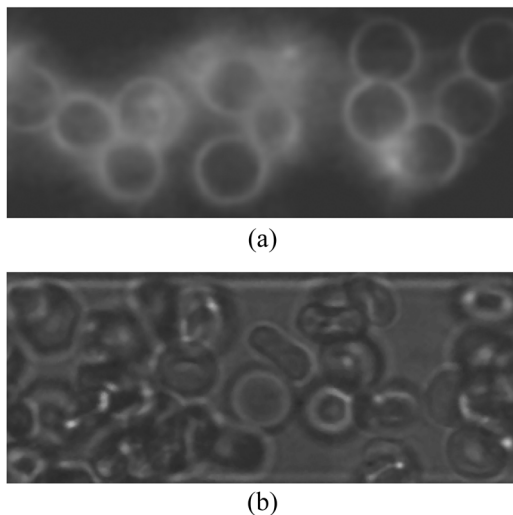


FIG. 2. Measured images of the particles of $8 \mu\text{m}$ diameter and rigidized red blood cells (RBCs) in the microchannel (center channel): (a) shows the particles measured by epi-illumination imaging, and (b) shows RBCs measured by transillumination imaging.

B. Sample preparation and measurement conditions

Micro-polystyrene particles with diameters of $5 \mu\text{m}$ and $8 \mu\text{m}$ (Microparticles GmbH, PS-R-5.0, PS-R-8.1) were used as particles in this study. For the RBCs, we fixed the RBCs and rigidized them using glutaraldehyde by following the next procedure. RBCs were collected from healthy volunteers and added 3.8 wt. % sodium citrate with the ratio of 9:1. The solution was centrifuged by 160 g at 25°C for 10 min. The supernatant, which is the platelet rich plasma, was removed, and the solution was further centrifuged by 900 g at 4°C for 15 min. The platelet poor plasma was removed, and the remaining concentrated RBCs were collected. The concentrated RBCs were suspended in 0.025% glutaraldehyde mixed phosphate buffered saline (PBS) solution for 1 h at room temperature to fix the biconcave shape of the RBC. The solution was centrifuged by 1000 g for 10 min, and the deposited RBCs were mixed in PBS solution.

The surface of the microchannel was coated by bovine serum albumin (BSA; Sigma-Aldrich Co., A2153-50G) to prevent the particles and RBCs to adhere to the wall. To apply the coating, the microchannel was filled with 10 wt. % BSA water solution for 60 min and then washed by flowing water to the channel by the pump. In addition to this, we also coated the particles by BSA to avoid the particle aggregation. The particles were suspended to 10 wt. % BSA water solution for 60 min. The solution was centrifuged by 2000 g for 1 min, and the BSA solution was removed. The deposited particles were then washed with water by pipetting. The coated particles were mixed with 10 wt. % BSA solution and supplied to the microchannel. On the other hand, the prepared rigidized-RBCs were separated and mixed to 0.1 wt. % sodium lauryl sulfate (Nacalai Co.) solution before used for the microchannel flow measurement.

The hematocrit (*Hct*) levels of the RBC solutions were examined once when the RBCs were treated with glutaraldehyde using the cell-counting plate. The *Hct* of the particles and RBCs was measured again before we supplied them to the channel and conducted the measurement. The *Hct* was varied under several conditions in the range of 9.2%–16.6%. It should be noted that some variation existed in the *Hct* for the cases in which the *Hct* of the particles and RBCs should be same for comparison and discussion. This is due to the fact that a portion of the particles and RBCs precipitated in the reservoir located upstream the channel. Another reason is that the *Hct* of the fluids in the three microchannels separated by the walls was not completely the same.

The flow rate was $0.6 \mu\text{l}/\text{min}$, and the average velocity at the center channel derived from the particle velocity was approximately 6 mm/s. The Reynolds numbers for the velocity of 6 mm/s and taking the characteristic lengths as the channel height and particle diameter of $8 \mu\text{m}$ were 2.1×10^{-1} and 6.0×10^{-2} , respectively. Therefore, the channel flow is in the laminar regime. The velocity distribution will follow the parabolic profile if the particles and RBCs do not affect the flow field. Furthermore, the particle velocity would be equal to the flow velocity as the particle Reynolds number is small. However, as the particle concentration increased, the particle velocity distribution deviated from the parabolic profile for some level. We will discuss this matter in Sec. IV A 5 where the effect of the velocity profile on the particle number distribution is considered.

Uncertainty analysis was conducted based on the American Society of Mechanical Engineers (ASME) standard. Measurement uncertainties of the Reynolds number were 10.4%, which was mainly

due to the uncertainty in the flow rate of the fluid flowing in the center channel after separating to three channels. The uncertainty of the hematocrit for the particles and RBCs during preparation was 16%. As mentioned above, further deviation was observed for the hematocrit measured at the channel due to the sedimentation at the reservoir. The uncertainty of the measured number density will be shown by error bars in the graph for the RBCs.

III. NUMERICAL MODEL

A. Governing equation

The conservation equation of the particle number density ϕ solved in this study consists of the convection and diffusion terms as shown in the following equation:

$$u_p \frac{\partial \phi}{\partial x} + \frac{\partial}{\partial y} ((v_c + v_f)\phi) = 0, \quad (1)$$

where u_p is the streamwise velocity of the particle. v_c is the migration velocity of the particles in the spanwise direction related to the particle-particle collision. v_f is the migration velocity attributed to the fluid dynamic force exerted on the particle. The product of the particle migration velocity and particle number density will give us the flux of particle concentration, N . Therefore, the flux generated by v_c and v_f can each be represented as $N_c = v_c\phi$ and $N_f = v_f\phi$.

The particle streamwise velocity u_p is considered to trace the flow velocity as the particle Reynolds number is small. We then assume that the flow in the channel is not affected by the particles and gives the Poiseuille flow distribution as the channel Reynolds number is small ($Re = 2.1 \times 10^{-1}$). This velocity profile is used for u_p in the channel spanwise direction. However, as mentioned previously, the particle velocity does not follow the parabolic profile when the particle concentration is large. We will discuss the particle velocity profile for this case in Sec. IV A 5, and the particle velocities measured by the experiment are applied to the computation to evaluate the effects on the particle concentration distribution.

Equation (1) is solved using the discretizing method. The convection term is discretized using the 1st order upwind scheme. The second term on the left-hand side of Eq. (1) for the flux of particle concentration in the spanwise direction is discretized using the 2nd order central difference scheme.

B. Collision model

Collision between two particles occurs when the streamwise velocities of the two are different and their motion path overlaps. The velocity difference can be represented by the product of the characteristic length and the shear rate: namely, the product of the distance between the two particles l_p and the local velocity gradient (shear rate) $\dot{\gamma}$. The collision rate can be obtained by multiplying this value with the number density of the opposing particle. The particles in collision will move in opposite directions with the distance equal to the overlapping length of the particles, which will be identical to the distance between the particle centers l_p . Therefore, the displacement of particles per time, which can be considered as the particle migration velocity, will be as expressed in the following equation:

$$v_c = -Kl_p^2 \nabla (|\dot{\gamma}| \phi), \quad (2)$$

where K is the constant of the migration velocity. Therefore, the flux of the ϕ in the spanwise direction will be $N_c = v_c\phi = -Kl_p^2 \phi \nabla (|\dot{\gamma}| \phi)$.

The above relationship is described in a generalized form. The velocity difference between the particles in collision and the distance between the particles (overlapping length) change depending on the relative positions of the particles. Therefore, we will use the velocities of the two particles in collision to calculate the velocity difference in this study. We will then derive the average spanwise migration velocity v_c for the particle of interest by integrating the value of each particle colliding with it over the collision area as follows:

$$v_c = K \int_S l_p(y, s) |u_p(y + s) - u_p(y)| \phi(y + s) 2\sqrt{d^2 - s^2} ds, \quad (3)$$

where s is the distance between the particle of interest located at the position of y and the opposing particle for collision. $l_p(y, s)$ is set equal to s . The sign of v_c is defined depending on which side of the particle Eq. (3) is integrated.

K is set as 0.04 (the unit will be inverse of ϕ) in the computation based on the comparison with the measurement. As will be shown in Sec. IV, measurement of the particle number density distribution was conducted over several conditions for the hematocrit, particle diameter, and streamwise position. We varied the value of K and defined it so that the difference between the distributions of the measurement and computation is minimum.

C. Effects of fluid dynamic force and Brownian motion

The fluid dynamic force is exerted on the particle when placed in shear flow, and the lift force tends to move the particle toward a certain position in the normal direction of the wall. The distribution of the lift force exerted on the particle by the flow field can differ by the Reynolds number. Schonberg and Hinch showed that the focusing position of the particles approaches the channel wall as the channel Reynolds number increases.²² However, the position converges to a certain value for the low Reynolds number condition. Although the number is not clearly shown in their results, the position does not vary significantly with the Reynolds number in the level of the Reynolds number smaller than one. To give the lift force of the particle in quantitative values, we will use the relationship between the lift force and flow velocity presented by Ho and Leal.²⁰ Ho and Leal measured the lift force applied to the particle in the Couette and Poiseuille flow of a two-dimensional incompressible Newtonian fluid. We applied this force to Stokes' law to derive the apparent particle migration velocity represented as follows:

$$v_f = \frac{\rho U_m^2 d^3}{48\pi\mu w^2} f(y), \quad (4)$$

where $f(y)$ is the normalized force in relation to the lateral position of the particle. ρ and μ are the fluid density and viscosity, respectively. U_m is the cross-sectional average velocity of the flow. d and w are the particle diameter and channel width, respectively. The flux of particles in the spanwise direction in the channel is, thus, the product of this migration velocity by the particle concentration, $N_f = v_f\phi$. This is applied to the particle concentration conservation equation shown in Eq. (1).

To evaluate the Brownian motion effect on the particle concentration, the Péclet number Pe is calculated using the particle

diffusion coefficient derived from the Stokes–Einstein equation. Pe for particles of $8\ \mu\text{m}$ is $Pe = 5.4 \times 10^8$ if we take the characteristic length as $6000\ \mu\text{m}$. The Pe is very large, and the displacement distance of particles in the spanwise direction owing to the Brownian motion for the streamwise length of $6000\ \mu\text{m}$ is $0.36\ \mu\text{m}$. Therefore, the Brownian motion effect is not included in the present model.

D. Red blood cell (RBC) modeling

As described in the Introduction, RBCs differ from solid particles as the former show a biconcave shape, possess deformability, and take a tank treading motion under shear flows. Among these effects, the biconcave shape and rotational motion of the RBC in a shear flow are focused in this study as we used rigidized RBCs. One of the effects of the biconcave shape is the difference in the collision rate of the RBCs. The overlapping area and the displacement length of the two cells in collision will depend on the attack angles of the RBCs against the main flow. We assumed that the attack angles of the RBCs have equal probability when the two RBCs collide. We then integrate the probability of the collision between the RBCs over the combination of the attack angles of the RBCs. This variable is defined as $\alpha(s)$ and is derived for each distance of s between the centers of the RBCs. The $\alpha(s)$ is applied to Eq. (3) as the correction factor. The profile of the correction factor $\alpha(s)$ in relation to the particle-particle distance s is shown in Fig. 3.

In addition to the collision rate of the RBC due to the translation motion in the streamwise direction, the RBC rotation caused by the vorticity in the shear flow can affect the collision rate and displacement in a dynamic manner. If the rotation speed is high, the probability of collision and the momentum transfer between the RBCs in collision can increase. To examine the effect, we will consider the ratio between the time required for the RBCs to collide, t_c , and the time for the RBC to rotate, t_r , t_r/t_c . The value of t_c is obtained by deriving the time required for the RBC to move the distance equal to the major axis of the RBC with the velocity difference between the two RBCs in collision. This can be simplified as $1/\dot{\gamma}$. The rotation period of an ellipsoid in shear flow is used for t_r which is based on the flow vorticity at the location of the RBC center.⁵¹ The ratio was $t_r/t_c = 26.7$ and is larger than unity. Therefore, the effect of rotating motion during collision on the collision rate is neglected in this study.

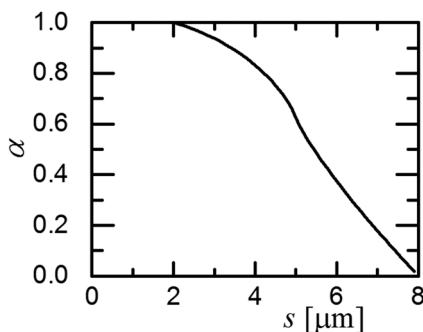


FIG. 3. Correction factor $\alpha(s)$ integrating the probability of the collision over the attack-angle of the two RBCs in collision: s is the distance between the centers of the RBCs in collision.

E. Wall effect

As the particle size becomes comparable with the channel size, we cannot treat particles as mass points and should consider the effect of their diameter. In this case, the relationship between the wall and the particle plays an important role in the number density distribution of the particles and RBCs in the channel. As the position of the particles and RBCs approaches the channel wall, the overlapping area for particles in collision and the displacement length after collision decrease on the channel side. Therefore, the collision rate and migration length show an asymmetric distribution. To apply this modification to the model expressed in Eq. (3), the integrating area is corrected as $(w - d)/2 - |y|$. w is the channel width. Similarly, as the wall will limit the particle and RBC migration, the displacement length in Eq. (3) is limited to the distance from the particle center to the wall.

In the RBC case, we additionally considered the effect of interaction between the RBC and the wall due to the RBC rotation. The rigidized RBC rotates in the flow due to the vorticity. The long axis of the biconcave-shape RBC located close to the channel wall contacts the wall during rotation. This makes the RBC detach from the wall as was observed in the measurement. The migration velocity of the RBC moving away from the wall due to this contact can be expressed by the product of the collision rate with the wall n_w and the displacement length l_d . We assume that n_w is proportional to the rotating velocity which can be expressed as the local vorticity ω . As ω is equal to the shear rate $\dot{\gamma}$ for the condition of the present study, we thus obtain

$$n_w = K_w \dot{\gamma}. \tag{5}$$

The migration velocity and flux of the particle number density ϕ will be as follows:

$$v_w = K_w l_d \dot{\gamma}, \tag{6}$$

$$N_w = K_w l_d \dot{\gamma} \phi. \tag{7}$$

We assume that the RBC in collision to the wall will move to the position where the distance of the RBC center to the wall is equal to the radius of the long axis of the RBC. Thus, l_d is set equal to the difference between the distance of the RBC center from the wall and the RBC's radius of the long axis. Constant K_w was set as $K_w = 5 \times 10^{-5}$.

IV. RESULTS AND DISCUSSION

A. Particle concentration distribution

1. Measurement results and comparison with computation

Figure 4 shows the number density ϕ distributions in the channel spanwise direction for particles with a diameter of $8\ \mu\text{m}$. Figures 4(a) and 4(b) show the results for particles suspended in fluids of $Hct = 11.7\%$ and 16.6% , respectively. In each figure, the distributions measured at the streamwise locations of $x = 0, 3000,$ and $6000\ \mu\text{m}$ are shown. $\bar{\phi}$ is the value of ϕ averaged in the spanwise direction.

The $\phi/\bar{\phi}$ distribution shows a uniform profile at the inlet of the center channel ($x = 0\ \mu\text{m}$), except in the region adjacent to the channel wall. In the near-wall region at $x = 0\ \mu\text{m}$, $\phi/\bar{\phi}$ shows a large value,

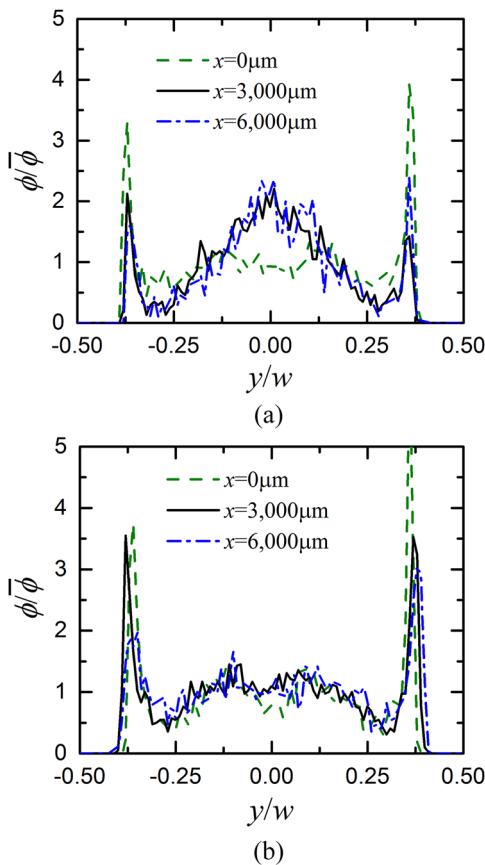


FIG. 4. Particle number density distribution in the channel spanwise direction. Measurement results for particles of diameter $d = 8 \mu\text{m}$ at different streamwise locations and Hct . (a) Hematocrit $Hct = 11.7\%$. (b) Hematocrit $Hct = 16.6\%$.

which is generated by the particles colliding with the leading edge of the partition walls of the channel. The colliding particles will enter either the center or the lateral channels. The particles colliding with the leading edge of the wall will flow along the wall of the center channel. Therefore, the number of particles in contact with the wall increases at the inlet. As the channel width is small in the present study, this effect becomes relatively large.

At $x = 3000 \mu\text{m}$, $\phi/\bar{\phi}$ increases in the region close to the channel center, whereas the maximum value near the wall decreases. At $x = 6000 \mu\text{m}$, $\phi/\bar{\phi}$ shows a distribution similar to that of $x = 3000 \mu\text{m}$, indicating that the effect of the inlet profile is reduced and the $\phi/\bar{\phi}$ distribution has developed to a certain degree.

The $\phi/\bar{\phi}$ distribution with $Hct = 16.6\%$, shown in Fig. 4(b), has a trend similar to that in the case of $Hct = 11.7\%$; namely, $\phi/\bar{\phi}$ around the center region increases, while the peak at the wall decreases in the downstream region, and the distribution shows little difference at $x = 6000 \mu\text{m}$. The $\phi/\bar{\phi}$ distribution at the channel centerline is smaller than those in the surrounding area. Therefore, in this case, two peaks are generated near the centerline.

Figure 5 shows the results of $\phi/\bar{\phi}$ distribution for the case of particles with a diameter of $5 \mu\text{m}$ at the concentration of $Hct = 9.2\%$.

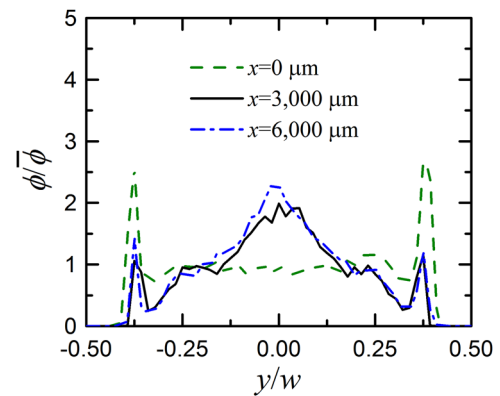


FIG. 5. Particle number density distribution for particles of diameter $d = 5 \mu\text{m}$. Measurement results for $Hct = 9.2\%$ at different streamwise locations.

The $\phi/\bar{\phi}$ distribution shows a maximum value at the centerline and near-wall region, which is similar to the case for particles of $8 \mu\text{m}$ at $Hct = 11.7\%$, shown in Fig. 4(a). A difference is, however, observed in the region between the centerline and the wall where a third peak additionally appears at $y/w \sim 0.25$. This is attributed to the spacing generated between the two highly concentrated regions of particles located at the channel center and at the wall as the particle size decreases. This space allows the particles to enter and generate another concentration peak. Later, we will discuss this using the computational results.

The numerical modeling of the particle number density $\phi/\bar{\phi}$ distribution is conducted by solving Eq. (1) with the experimental conditions applied to the computation, i.e., the particle diameter, average particle number density (hematocrit), channel width of $28 \mu\text{m}$, and flow average velocity of 6 mm/s .

Figure 6 shows the particle number density $\phi/\bar{\phi}$ distributions obtained by the computation for particles of 5 and $8 \mu\text{m}$ diameter. The measurement results shown in Figs. 4 and 5 are depicted in the figure for comparison. In Fig. 6(a), the distribution shows two high-concentration regions, one located at the channel center and the other near the channel walls. Evaluating the concentration flux by verifying the values of each model term in the equation, the large $\phi/\bar{\phi}$ observed at the center is attributed to the parabolic profile of the velocity distribution. With the large shear rate located at the channel wall and decreasing to zero at the channel center, the collision rate of particles shows a larger value in the wall side and the particles migrate to the center. This characteristic is consistent with those of particles in cylinders or channel flows reported by Lei *et al.*³

The other peak of large $\phi/\bar{\phi}$ appearing at the channel wall is due to the zero collision of particles at the wall side. The peak is located close to $|y/w| \sim 0.36$, which is the position where the particle center is located when the particle is attached to the wall. If the particle approaches the wall and the distance between the particle center and the wall is smaller than three times the particle radius, the area of particle collisions in the wall side is smaller. Once the particle attaches to the wall, no collision will occur at the wall side. The particle is pressed to the wall and particle migration will depend on the fluid dynamic force.

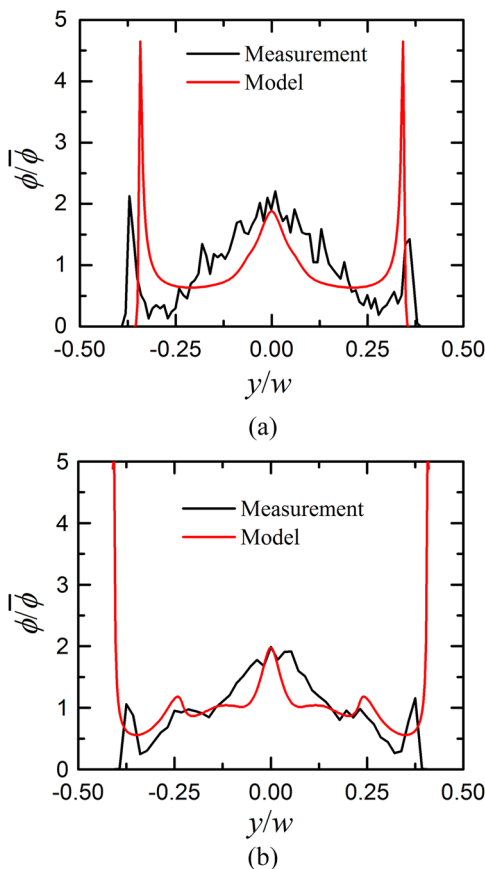


FIG. 6. Particle number density distribution of model and measurement for particles of $d = 5$ and $8 \mu\text{m}$ compared at $x = 3000 \mu\text{m}$. (a) $d = 8 \mu\text{m}$, $Hct = 11.7\%$. (b) $d = 5 \mu\text{m}$, $Hct = 9.2\%$.

Thus, the particles concentrate on the channel center and wall as they flow downstream of the channel, which agrees well with the measurement. In the present study, the width of the channel is of the order of several particle diameters, and the particle Reynolds number is $\sim O(0.01)$. The collision effect is larger compared with the fluid dynamic force, especially when the hematocrit is large. As described in the work of Lei *et al.*,³ when the channel width value is smaller than two times the RBC diameter, $\phi/\bar{\phi}$ shows maximum values near the wall while $\phi/\bar{\phi}$ at the centerline decreases. This is attributed to the lack of space for particles to locate at that position. As the channel width increases, the region of large $\phi/\bar{\phi}$ is generated also at the centerline, which agrees well with the present results.

For $d = 5 \mu\text{m}$ and $Hct = 9.2\%$ shown in Fig. 6(b), the maximum values are observed at the channel center and near-wall region. The difference between the case with $d = 8 \mu\text{m}$ shown in Fig. 6(a) is that a third peak is observed in the position of $y/w \sim 0.25$, which is located between the peaks of $\phi/\bar{\phi}$ at the centerline and channel wall. This agrees well with the measurement, and the cause will be discussed shortly with the effects of particle size on the particle concentration distribution.

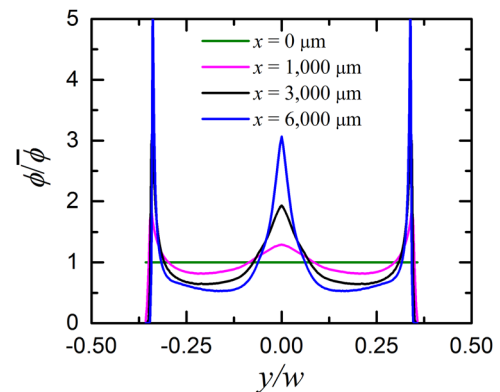


FIG. 7. Effects of the streamwise position on particle number density distribution in computation (particles of $d = 8 \mu\text{m}$, $Hct = 10\%$).

2. Streamwise location effect

Figure 7 shows how the particle number density distributions $\phi/\bar{\phi}$ change in the streamwise direction in the computation for particles with diameter $d = 8 \mu\text{m}$ and $Hct = 10\%$. The flat distribution of $\phi/\bar{\phi}$ at the inlet changes as the particles flow downstream, having the particle concentration increase at the centerline and near-wall regions. The profile still is in a developing stage at $x = 6000 \mu\text{m}$ where the distribution differs with that at $x = 3000 \mu\text{m}$. This characteristic differs from the measurement shown in Fig. 4(a), where the particle concentration at $x = 3000$ and $6000 \mu\text{m}$ showed the same distribution. As the model only considers the effects of the particle–particle collision, fluid dynamic force, and wall, $\phi/\bar{\phi}$ continuously increases at the centerline and near-wall regions until the force based on these effects becomes balanced. The particles themselves are treated as mass points, and the maximum packing ratio is not considered in the computation. Furthermore, the effects of the particles on the surrounding fluid, including the apparent viscous change discussed in the model of Phillips *et al.*,⁴¹ can become significant for the region where the particle concentration is high. These factors can affect the particle spanwise motion and decrease the spanwise velocity and displacement or create a limit for the value of the local particle concentration. These effects should be introduced in the model, especially for particle-packed flows, and evaluated by comparing them with the experiment.

3. Particle size effects

Figure 8 shows the $\phi/\bar{\phi}$ distributions for particles of diameters $d = 3 \mu\text{m}$, $5 \mu\text{m}$, $8 \mu\text{m}$, and $10 \mu\text{m}$. For $d = 8$ and $10 \mu\text{m}$, the distributions show a similar trend having their maximum peaks located at the centerline and near-wall region. The difference mainly appears at the y/w position of the peak near the wall, where the center of the particle will have a distance from the wall according to the diameter. A larger peak of $\phi/\bar{\phi}$ is also obtained for larger d as the collision area (overlapping area of particles in collision) and the displacement due to collision increases with d .

For $d = 5 \mu\text{m}$, a third peak is observed near the middle of the centerline and wall. This distribution agrees well with the measurement, as can be seen in Fig. 6(b). The main cause of this third peak is attributed to the wall effect and the local maximum of $\phi/\bar{\phi}$ in the

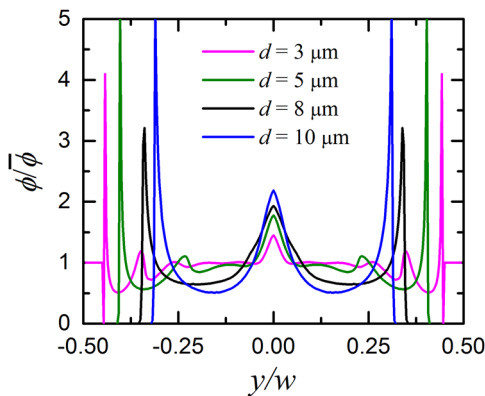


FIG. 8. Effects of the particle diameter on particle number density distribution in computation (particles of $Hct = 10\%$ at $x = 3000 \mu\text{m}$).

near-wall region. For particles located close to the wall, the collision area at the wall side and the displacement toward the wall is reduced. The migration velocity v_c has the direction toward the wall in the near-wall region and the direction toward the centerline in the region apart from the wall due to the effect of large particle concentration near the wall. The effect of this large $\phi/\bar{\phi}$ in the near wall region on v_c is significant, but it will sharply decay as the particles are located outside of the area overlapping with this large $\phi/\bar{\phi}$ region. The position of the third peak is where the effect of this maximum value in the near-wall region decays. This produces a local drop in v_c and generates the third maximum value. In the case of $d = 3 \mu\text{m}$, a fourth peak is generated in the $\phi/\bar{\phi}$ distribution due to a similar reason: namely, v_c largely changes at the location of the fourth peak by the effect of the other large $\phi/\bar{\phi}$ region observed in the wall side. This effect of the maximum value in the near-wall region does also exist for a large particle with the diameters of $d = 8$ and $10 \mu\text{m}$. However, the effect appears near the centerline, and it is not as noticeable as in the case of $d = 3$ and $5 \mu\text{m}$ where the third and fourth peaks are generated.

4. Hematocrit effects

The effect of the overall Hct on the $\phi/\bar{\phi}$ distribution is shown in Fig. 9, where flows with $Hct = 5\%$, 10% , 15% , and 20% are discussed. An increase in the overall Hct increases the local particle concentration and the resulting collision rate. This directly leads to the increase in the particle concentration flux. Therefore, the maximum values of $\phi/\bar{\phi}$ increase as Hct increases. Meanwhile, the measurement results with $Hct = 11.7\%$ and 16.6% , which are also shown in the figure for comparison, show a different trend, namely, a higher Hct condition results in a moderate distribution and $\phi/\bar{\phi}$ at the center shows a moderate minimum. To examine the reason of this disagreement one step further, the effects of the velocity profile are evaluated in Sec. IV A 5.

5. Flow velocity profile effects

Comparing the results of the measurement and the numerical model, the distributions show a quantitative deviation. As discussed previously, this can be attributed to the effects of the

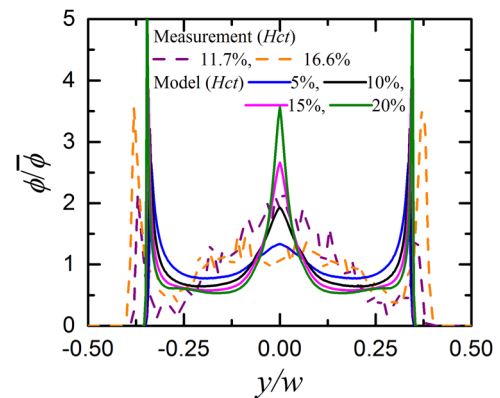


FIG. 9. Effects of overall hematocrit Hct on particle number density distribution in computation (particles of $d = 8 \mu\text{m}$ at $x = 3000 \mu\text{m}$).

particles on the local flow and the limitation of the particle density for high-concentration flows. In addition, the highly concentrated particles can change the streamwise velocity distribution of the flow and particles in the channel: namely, the velocity profile can differ from the parabolic distribution which is applied to the computation. The different velocity distribution affects the collision and mobility of the particles and changes the particle concentration distribution. To evaluate this effect, we measured the streamwise velocity of the particles for the cases of a particle diameter of $8 \mu\text{m}$ with $Hct = 10\%$ and 15.9% . The particle velocity distribution was then applied to the computation to calculate the particle concentration distribution.

Figure 10 shows the distributions of the particle streamwise velocities u_p . Figures 10(a) and 10(b) represent the results for the cases of Hct of 10% and 15.9% , respectively. The parabolic distribution of the flow in a channel derived based on the flow rate is superimposed in the figure.

In Fig. 10(a), u_p takes a distribution similar to a parabolic one. However, some deviation is observed at the centerline and in the near wall region where u_p is smaller compared with the values of the parabolic profile. In the case of higher Hct condition shown in Fig. 10(b), the effect of the particles on u_p is significant and u_p shows a plateau near the centerline. As Hct increases, the collision rate increases and gives an additional momentum transfer including the streamwise components over the spanwise region. This changes the velocity distribution to become uniform, as shown in the figure.

Figure 11 shows the particle concentration distribution for the case of using the velocity profile shown in Fig. 10 in the computation. In Fig. 11(a), the $\phi/\bar{\phi}$ distribution of $Hct = 10\%$ shows a broader distribution at the center of the channel compared with those shown in Fig. 6(a). The velocity distribution is relatively flat at the channel center, and the migration velocity of the particle concentration in this region decreases. In the case with $Hct = 16.6\%$ shown in Fig. 11(b), the $\phi/\bar{\phi}$ distribution matches well with the measurement, compared with the case shown in Fig. 9: the decrease in $\phi/\bar{\phi}$ at the centerline is presented and the distribution shows a flat pattern. The velocity distribution shown in Fig. 10(b) gives a plateau in the center region. The flat profile decreases the migration velocity of the particle concentration. Thus, $\phi/\bar{\phi}$ increases first at the location where

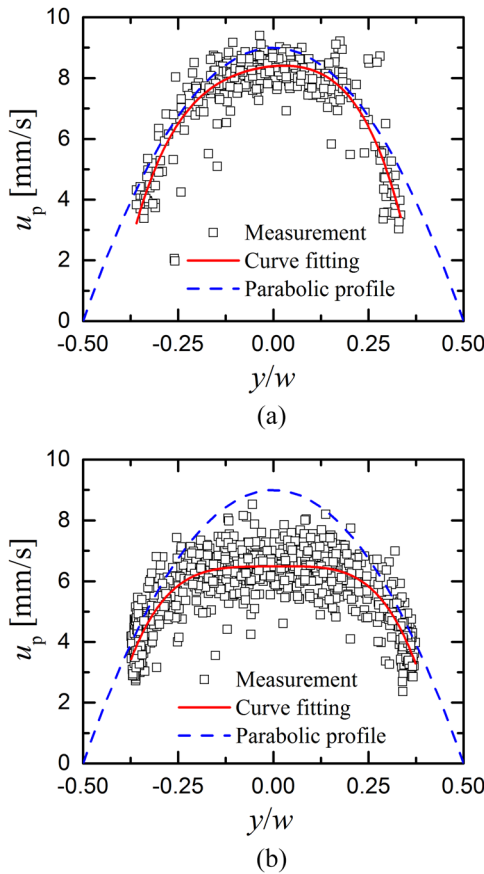


FIG. 10. Streamwise velocity distribution of the particles u_p at $x = 3000 \mu\text{m}$ for particles with a diameter of $8 \mu\text{m}$ and a concentration of $Hct = 10\%$ and 15.9% . (a) $d = 8 \mu\text{m}$, $Hct = 10\%$. (b) $d = 8 \mu\text{m}$, $Hct = 15.9\%$.

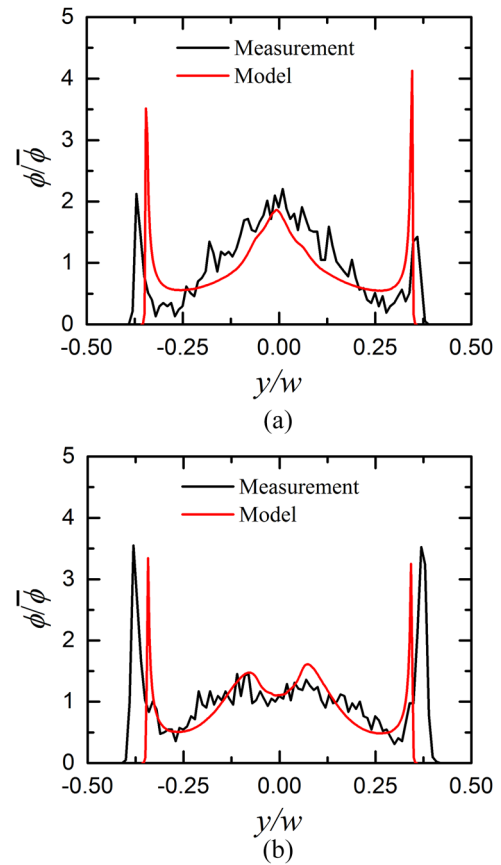


FIG. 11. Effects of the velocity profile on number density distribution at $x = 3000 \mu\text{m}$. (a) $d = 8 \mu\text{m}$, $Hct = 11.7\%$. (b) $d = 8 \mu\text{m}$, $Hct = 16.6\%$.

the velocity gradient largely decreases and produces the two peaks located close to the centerline.

These results show that the velocity distribution should be carefully considered to predict the particle concentration distribution correctly especially for particle concentrated fluids.

B. Red blood cell concentration distribution

Figure 12 shows the $\phi/\bar{\phi}$ distribution of the RBCs measured for the case with $Hct = 10\%$. Figure 12(a) shows the measurement results with the results of the $8\text{-}\mu\text{m}$ particle case. In the figure, $\phi/\bar{\phi}$ distribution of the RBCs shows maximum values at the channel center and near-wall region, and additionally at the middle of these two positions, at $y/w \sim 0.3$. Therefore, the distribution differs from that of the $8\text{-}\mu\text{m}$ particles and is similar to that of the $5\text{-}\mu\text{m}$ particles. As the RBC is fixed to the biconcave shape and rotates in the channel flow, the effective diameter of the RBC for collision with the surrounding RBCs is smaller than $8 \mu\text{m}$. Therefore, the cell-cell collision characteristics resemble more closely to those of the $5\text{-}\mu\text{m}$ particles. Furthermore, the position of the maximum value in the near-wall region is located closer to the wall.

The $\phi/\bar{\phi}$ distribution of the model, in which the collision area is modified and the collision to the wall due to the RBC rotation is considered as described in Secs. III D and III E, is shown in Fig. 12(b) together with the measurement result. The third maximum value is produced in the distribution obtained by the computation. Furthermore, the position of the peak in the near-wall region is located closer to the wall compared to the $8\text{-}\mu\text{m}$ particle case and matches with that of the measurement. Thus, although the $\phi/\bar{\phi}$ distributions do not completely correspond with the measurements, they match with the measurement qualitatively, especially with respect to the number and locations of the maximum values.

We will now modify the parameters and evaluate their effects on the distribution to understand the tendency of the RBC motion and shape effects. Figure 13 shows the $\phi/\bar{\phi}$ distribution in the cases of different streamwise position and when α is varied. In Fig. 13(a), the maximum values $\phi/\bar{\phi}$ are observed at the center, the wall, and the middle of these two locations from the upstream region of the channel. The location of these peaks do not differ much through the channel. In Fig. 13(b), as α decreases, the particle concentration flux decreases owing to the small collision area and displacement length, and the distribution shows a flat distribution with maximum peaks located only near the wall. As α increases, the maximum values at the

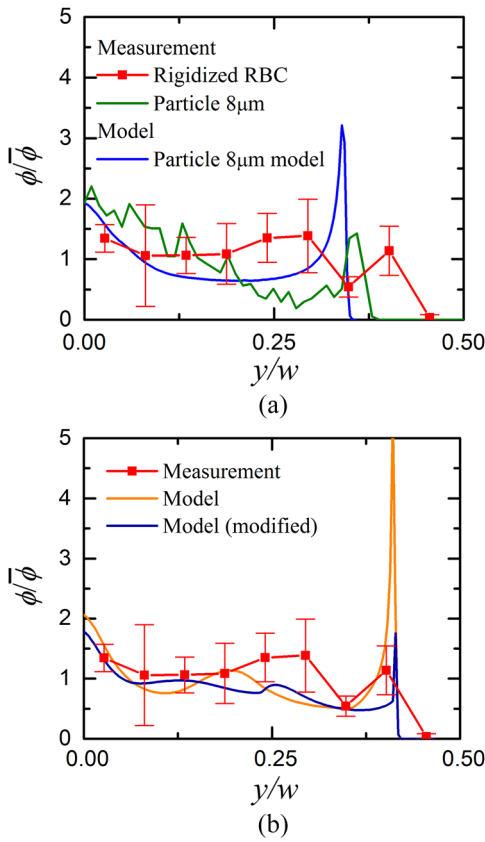


FIG. 12. Number density distribution for RBCs and comparison with the model. (a) RBCs vs particles. (b) Model for RBC.

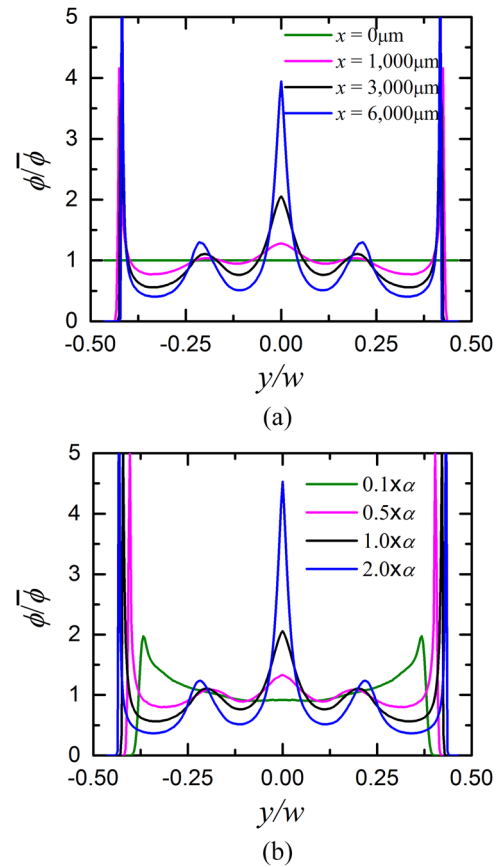


FIG. 13. Effects of the streamwise position (a) and model constant α (b) on number density distribution at $x = 3000 \mu\text{m}$ for RBCs of $Hct = 10\%$.

channel center and at $|y|/w \sim 0.2$ increase. As only the value of α is increased in a similar fashion and the area of collision is not changed, the location of the maximum values does not vary considerably as α changes.

Although not shown here, when v_w is varied, the effect is limited to the area close to the wall, in which the position of the maximum peak distances from the wall. In the present model, the additional migration velocity v_w is applied only to the RBC located in the area within a distance of $4 \mu\text{m}$ to the wall. The momentum of the rotation of the RBC colliding with the wall to the surrounding RBCs is not considered, and the propagation of the effect toward the center is not presented. Thus, the effect of v_w is limited in the near-wall region, and therefore, the reduction rate of the maximum value is also limited.

As the effects of the terms in the equation and the parameters have been characterized, we will now approximately modify the parameters and make the distribution become closer to the measured one to evaluate the effecting factors that should be further considered in the model. The range of the collision area was reduced from $8 \mu\text{m}$ to $5 \mu\text{m}$, and the coefficient for the wall detachment effect was increased by a factor of 20. The results are shown in Fig. 12(b) as the modified case. In this case, the position of the maximum values located between the channel center and the wall approaches that of

the measurement values. Furthermore, the maximum value located close to the wall decreases. Although a deviation still exists between the model and the measurement, and its adjustment exceeds the span of the present work, we may assume that the biconcave shape and rotation of the RBC further reduce the effective diameter of the RBC. Furthermore, a large detachment from the wall should be applied to overcome the decrease in the effective diameter. This could be considered as a problem of the present model, which needs to be solved in a future work.

V. CONCLUSIONS

In this study, the number density ($\phi/\bar{\phi}$) distributions of particles and RBCs in a microchannel flow were investigated to evaluate the effects of the small channel width on the spanwise concentration flux of the particles and RBCs, especially considering the effects of the particle-particle (cell-cell) collision. The particles became concentrated at the near-wall region due to the wall effects on the collision area and migration distance of the particles and cells. The increase of the hematocrit produced a flat velocity profile at the channel center which reduced the particle migration velocity in that region and the maximum value of $\phi/\bar{\phi}$. As the ratio

between the particle diameter and channel width decreased, additional peaks appeared in the ϕ/ϕ distribution. The biconcave shape of the RBC gave a probability of the collision rate due to the change in the attack-angle of the RBC, which resulted in a smaller migration velocity. On the other hand, the rotation and collision of the RBCs with the channel wall decreased the maximum value at the near-wall region. The present model agreed reasonably well with the measurement, whereas the deviation between the concentration distributions of the model and measurement still exists for a certain level. The present model lacks in the consideration of the particle migration and RBC rotation effects on the fluid flow around the particle and RBC, rotational motion of the particle and RBC due to the collision, and the packing problem which limits the number of particles in the region of interest. These effects will reduce the migration velocity and produce a moderate distribution and decrease the maximum values that may improve the model to produce a distribution closer to the measurement. In addition to this, the normal RBCs possess deformability and show tank treading motion in the shear flow that will exert a different lift force on the RBCs. Therefore, it is necessary to take this effect into account for the model and compare them with the measurement further conducted as the future work.

ACKNOWLEDGMENTS

We thank Hideo Hirakata, MD, of Kyoto city hospital; Naoko Sugita, MD; and Kyo Inoue, MD, of the Graduate School of Medicine and Faculty of Medicine, Kyoto University, for their assistance in providing the blood samples and for their comments that greatly improved the manuscript. This work has been approved by the ethics committees of the Graduate School and Faculty of Medicine and the Graduate School of Engineering and Faculty of Engineering, Kyoto University. This work was supported by JSPS KAKENHI, Grant No. 15H03931.

REFERENCES

- N. Tateishi, Y. Suzuki, I. Cicha, and N. Maeda, "O₂ release from erythrocytes flowing in a narrow O₂-permeable tube: Effects of erythrocyte aggregation," *Am. J. Physiol.: Heart Circ. Physiol.* **281**, H448 (2001).
- D. A. Fedosov, W. Pan, B. Caswell, G. Gompper, and G. E. Karniadakis, "Predicting human blood viscosity *in silico*," *Proc. Natl. Acad. Sci. U. S. A.* **108**, 11772 (2011).
- H. Lei, D. A. Fedosov, B. Caswell, and G. E. Karniadakis, "Blood flow in small tubes: Quantifying the transition to the non-continuum regime," *J. Fluid Mech.* **722**, 214 (2013).
- D. Alizadehrad, Y. Imai, K. Nakaaki, T. Ishikawa, and T. Yamaguchi, "Quantification of red blood cell deformation at high-hematocrit blood flow in microvessels," *J. Biomech.* **45**, 2684 (2012).
- H. Zhao, E. S. G. Shaqfeh, and V. Narsimhan, "Shear-induced particle migration and margination in a cellular suspension," *Phys. Fluids* **24**, 011902 (2012).
- J. M. Sherwood, E. Kaliviotis, J. Dusing, and S. Balabani, "Hematocrit, viscosity and velocity distributions of aggregating and non-aggregating blood in a bifurcating microchannel," *Biomech. Model. Mechanobiol.* **13**, 259 (2014).
- Q. M. Qi and E. S. G. Shaqfeh, "Theory to predict migration and margination in the pressure-driven channel flow of blood," *Phys. Rev. Fluids* **2**, 093102 (2017).
- Q. M. Qui and E. S. G. Shaqfeh, "Time-dependent particle migration and margination in the pressure-driven channel flow of blood," *Phys. Rev. Fluids* **3**, 034302 (2018).
- J. L. McWhirter, H. Noguchi, and G. Gompper, "Flow-induced clustering and alignment of vesicles and red blood cells in microcapillaries," *Proc. Natl. Acad. Sci. U. S. A.* **106**, 6039 (2009).
- J. B. Freund and M. M. Orescanin, "Cellular flow in a small blood vessel," *J. Fluid Mech.* **671**, 466 (2011).
- A. Kumar and M. D. Graham, "Margination and segregation in confined flows of blood and other multicomponent suspensions," *Soft Matter* **8**, 10536 (2012).
- D. A. Reasor, Jr., M. Mehrabadi, D. N. Ku, and C. K. Aidun, "Determination of critical parameters in platelet margination," *Ann. Biomed. Eng.* **41**, 238 (2013).
- N. Takeishi, Y. Imai, T. Yamaguchi, and T. Ishikawa, "Flow of a circulating tumor cell and red blood cells in microvessels," *Phys. Rev. E* **92**, 063011 (2015).
- M. Faivre, M. Abkarian, K. Bickraj, and H. A. Stone, "Geometrical focusing of cells in a microfluidic device: An approach to separate blood plasma," *Biorheology* **43**, 147 (2006), <https://content.iospress.com/articles/biorheology/bir384>.
- D. Di Carlo, J. F. Edd, K. J. Humphry, H. A. Stone, and M. Toner, "Particle segregation and dynamics in confined flows," *Phys. Rev. Lett.* **102**, 094503 (2009).
- T. Kulrattanarak, R. G. M. van der Sman, C. G. P. H. Schroën, and R. M. Boom, "Classification and evaluation of microfluidic devices for continuous suspension fractionation," *Adv. Colloid Interface Sci.* **142**, 53 (2008).
- A. A. S. Bhagat, S. S. Kuntaegowdanahalli, and I. Papautsky, "Enhanced particle filtration in straight microchannels using shear-modulated inertial migration," *Phys. Fluids* **20**, 101702 (2014).
- K. Tatsumi, K. Kawano, H. Shintani, and K. Nakabe, "Analysis and measurement of dielectrophoretic manipulation of particles and lymphocytes using rail-type electrodes," *Med. Eng. Phys.* **38**, 24 (2016).
- G. Segre and A. Silberberg, "Behaviour of macroscopic rigid spheres in Poiseuille flow: Part 2. Experimental results and interpretation," *J. Fluid Mech.* **14**, 136 (1962).
- B. P. Ho and L. G. Leal, "Inertial migration of rigid spheres in two-dimensional unidirectional flows," *J. Fluid Mech.* **65**, 365 (1974).
- M. R. Maxey, "Equation of motion for a small rigid sphere in a nonuniform flow," *Phys. Fluids* **26**, 883 (1983).
- J. Schonberg and E. J. Hinch, "Inertial migration of a sphere in Poiseuille flow," *J. Fluid Mech.* **203**, 517 (1989).
- R. E. Hampton, A. A. Mammoli, A. L. Graham, and N. Tetlow, "Migration of particles undergoing pressure-driven flow in a circular conduit," *J. Rheol.* **41**, 612 (1997).
- M. Han and C. Kim, "Particle migration in tube flow of suspensions," *J. Rheol.* **43**, 1157 (1999).
- E. S. Asmolov, "The inertial lift on a spherical particle in a plane Poiseuille flow at large channel Reynolds number," *J. Fluid Mech.* **381**, 63 (1999).
- J.-P. Matas, J. F. Morris, and E. Guazzelli, "Inertial migration of rigid spherical particles in Poiseuille flow," *J. Fluid Mech.* **515**, 171 (2004).
- K. J. Humphry, P. M. Kulkarni, D. A. Weitz, J. F. Morris, and H. A. Stone, "Axial and lateral particle ordering in finite Reynolds number channel flows," *Phys. Fluids* **22**, 081703 (2010).
- M. Abbas, P. Magaud, Y. Gao, and S. Geoffroy, "Migration of finite sized particles in a laminar square channel flow from low to high Reynolds number," *Phys. Fluids* **26**, 123301 (2014).
- T. Fukuda, S. Takeuchi, and T. Kajishima, "Effects of curvature and vorticity in rotating flows on hydrodynamic forces acting on a sphere," *Int. J. Multiphase Flow* **58**, 292 (2014).
- T. Roth, L. Sprenger, S. Odenbach, and U. O. Häfeli, "Continuous form-dependent focusing of non-spherical microparticles in a highly diluted suspension with the help of microfluidic spirals," *Phys. Fluids* **30**, 045102 (2018).
- A. Shamloo and A. Mashhadian, "Inertial particle focusing in serpentine channels on a centrifugal platform," *Phys. Fluids* **30**, 012002 (2018).
- M. M. Reddy and A. Singh, "Shear-induced particle migration and size segregation in bidisperse suspension flowing through symmetric T-shaped channel," *Phys. Fluids* **31**, 053305 (2019).
- M. Abkarian, C. Lartigue, and A. Viallat, "Tank treading and unbinding deformable vesicles in shear flow: Determination of the lift force," *Phys. Rev. Lett.* **88**, 068103-1 (2002).
- T. M. Geislinger and T. Franke, "Hydrodynamic lift of vesicles and red blood cells in flow—From Fåhræus and Lindqvist to microfluidic cell sorting," *Adv. Colloid Interface Sci.* **208**, 161 (2014).

- ³⁵D. Abreu, M. Levant, V. Steinberg, and U. Seifert, "Fluid vesicles in flow," *Adv. Colloid Interface Sci.* **208**, 129 (2014).
- ³⁶A. H. Karnis, L. Goldsmith, and S. G. Mason, "The kinetics of flowing dispersions: I. Concentrated suspensions of rigid particles," *J. Colloid Interface Sci.* **22**, 531 (1966).
- ³⁷I. M. Krieger, "Rheology of monodisperse latices," *Adv. Colloid Interface Sci.* **3**, 111 (1972).
- ³⁸C. J. Koh, P. Hookham, and L. G. Leal, "An experimental investigation of concentrated suspension flows in a rectangular channel," *J. Fluid Mech.* **266**, 1 (1994).
- ³⁹H. Iddir and H. Arastoopour, "Modeling of multitype particle flow using the kinetic theory approach," *AIChE J.* **51**, 1620 (2005).
- ⁴⁰D. Leighton and A. Acrivos, "The shear-induced migration of particles in concentrated suspensions," *J. Fluid Mech.* **181**, 415 (1987).
- ⁴¹R. J. Phillips, R. C. Armstrong, and R. A. Brown, "A constitutive equation for concentrated suspensions that accounts for shear-induced particle migration," *Phys. Fluids A* **4**, 30 (1992).
- ⁴²S. R. Subia, M. S. Ingber, L. A. Mondy, S. A. Altobelli, and A. L. Graham, "Modelling of concentrated suspensions using a continuum constitutive equation," *J. Fluid Mech.* **373**, 193 (1998).
- ⁴³A. S. Sangani, A. Acrivos, and P. Peyla, "Roles of particle-wall and particle-particle interactions in highly confined suspensions of spherical particles being sheared at low Reynolds numbers," *Phys. Fluids* **23**, 083302 (2011).
- ⁴⁴J. R. Agudo, S. Dasilva, and A. Wierschem, "How do neighbors affect incipient particle motion in laminar shear flow?," *Phys. Fluids* **26**, 053303 (2014).
- ⁴⁵P. Pham, B. Metzger, and J. E. Butler, "Particle dispersion in sheared suspensions: Crucial role of solid-solid contacts," *Phys. Fluids* **27**, 051701 (2015).
- ⁴⁶J. Hu and Z. Guo, "Effect of interaction between a particle cluster and a single particle on particle motion and distribution during sedimentation: A numerical study," *Phys. Fluids* **31**, 033301 (2019).
- ⁴⁷R. B. Reboucas, I. R. Siqueira, P. R. de Souza Mendes, and M. S. Carvalho, "On the pressure-driven flow of suspensions: Particle migration in shear sensitive liquids," *J. Non-Newtonian Fluid Mech.* **243**, 178 (2016).
- ⁴⁸X. Grandchamp, G. Coupier, A. Srivastav, C. Minetti, and T. Podgorski, "Lift and down-gradient shear-induced diffusion in red blood cell suspensions," *Phys. Rev. Lett.* **110**, 108101 (2013).
- ⁴⁹S. Inoue and K. R. Spring, *Video Microscopy: The Fundamentals*, 2nd ed. (Plenum Press, New York, 1997).
- ⁵⁰J. Schindelin, I. Arganda-Carreras, E. Frise, V. Kaynig, M. Longair, T. Pietzsch, S. Preibisch, C. Rueden, S. Saalfeld, B. Schmid, J. Y. Tinevez, D. J. White, V. Hartenstein, K. Eliceiri, P. Tomancak, and A. Cardona, "Fiji: An open-source platform for biological-image analysis," *Nat. Methods* **9**, 676 (2012).
- ⁵¹G. B. Jeffery, "The motion of ellipsoidal particles immersed in a viscous fluid," *Proc. R. Soc. A* **125**, 161 (1922).